RSC Advances

PAPER

View Article Online
View Journal | View Issue

Cite this: *RSC Adv.*, 2023, **13**, 19079

Mesoporous silica nanoparticles with dual-targeting agricultural sources for enhanced cancer treatment *via* tritherapy†

Yu-Ya Huang,[a] Zui-Harng Lee,[a] Kai-Chi Chang, *[b] Zhi-Yuan Wu,[a] Cheng-Chang Lee,[a] Min-Hsuan Tsou[a] and Hsiu-Mei Lin *[acd]

Received 30th March 2023
Accepted 29th May 2023

DOI: 10.1039/d3ra02068a

rsc.li/rsc-advances

In this study, we introduced dual-targeting folic acid (FA) and hyaluronic acid (HA) modified on the surface of rice husk mesoporous silica nanoparticles (rMSNs). The rMSNs were employed as a drug delivery system loaded with camptothecin (CPT) as a model drug, Eu^{3+} ions as a photosensitizer for photodynamic therapy (PDT), bismuth (Bi) for photothermal therapy (PTT), and Gd^{3+} ions for magnetic resonance imaging (MRI) to develop novel nanoparticles, rMSN-EuGd-Bi@CPT-HA-FA, with dual-targeted function and triple therapy for cancer treatment. The results of the cell cytotoxicity experiment showed that the A549 cancer cells had a survival rate of approximately 35% when treated with 200 μg mL^{-1} of rMSN-EuGd-Bi@CPT-HA-FA under 808 nm irradiation for 15 min. The dual-targeted function and synergistic treatment of CPT, PTT, and PDT were also responsible for the 20% survival rate of the A549 cancer cells treated with 200 μg mL^{-1} of rMSN-EuGd-Bi@CPT-HA-FA under 808 nm irradiation for 30 min. The results showed that rMSN-EuGd-Bi@CPT-HA-FA can effectively combine chemotherapy (through CPT), PDT, and PTT for cancer treatment.

1. Introduction

Cancer is one of the leading causes of death globally, and chemotherapy remains the primary treatment method.[1] In conventional medicine, cancer cells undergo apoptosis; however, the effects of these treatments are nonselective and nonspecific, and healthy normal cells are also damaged, which causes several side effects, such as hair loss, vomiting, and cancer pain.[2–4] In recent years, various emerging cancer therapy methods have been reported to improve traditional drug treatments, such as photodynamic therapy (PDT),[5] photothermal therapy (PTT)[6] and nanoparticle drug delivery systems.[7] PDT is a form of phototherapy involving light and a photosensitizer used in conjunction with oxygen to induce cell death. Recent studies have reported that incorporating Eu^{3+} ions as photosensitizing agents into nanoparticles and irradiating with near-infrared light can cause the materials to produce reactive oxygen species (ROS), demonstrating that nanoparticles are suitable for PDT.[8] PTT refers to the use of infrared wavelengths for the treatment of various medical conditions, including cancer. Recently, bismuth (Bi)-based nanoparticles have been reported for PTT in cancer treatment.[9] The development trend is mostly to use a combination of two or more therapies, which decreases the dosage of drugs used and reduces the damage and side effects of drugs to normal cells.

Nanoparticle drug delivery systems in combination with multiple therapies can overcome the current problems and improve therapeutic efficacy through a targeting system to deliver drugs *in vivo* to target specific areas while passive targeting is employed, known as the enhanced permeability and retention effect (EPR effect),[10] or active targeting.[11] Regarding the physiology of cancer cells, certain receptors on the cell membrane are highly expressed compared with those on the normal cell membrane. Hence, functional molecules can be modified with folic acid (FA)[12] and hyaluronic acid (HA).[13] The receptors to be exploited are the folate receptor and CD44. It is worth mentioning that HA is not only a targeting molecule for tumor cells but also a nanoparticle gatekeeper owing to its polymer properties.[14] Besides, in previous research, the high-molecular weight HA (1.5–1.8 MDa) can have both gatekeeper and targeted functions.[15]

In this study, we employed mesoporous silica nanoparticles (MSNs) as drug carriers for combination therapies. To enhance the advantages of traditional MSNs, instead of tetraethyl orthosilicate, we used rice husks and recycled agricultural waste as the natural silica source, which also makes it more

[a]National Taiwan Ocean University, Department of Bioscience and Biotechnology, No. 2, Beining Rd., Zhongzheng Dist., Keelung City 202, Taiwan, Republic of China. E-mail: hmlin@mail.ntou.edu.tw; Fax: +886-2-2462-2192; Tel: +886-2-2462-2192

[b]National Taiwan Ocean University, Bachelor Degree Program in Marine Biotechenology, Taiwan

[c]National Taiwan Ocean University, Center of Excellence for the Oceans, Taiwan

[d]National Taiwan Ocean University, Center of Excellence for Ocean Engineering, Taiwan

† Electronic supplementary information (ESI) available. See DOI: https://doi.org/10.1039/d3ra02068a

environmentally friendly. After calcination, rice husks have an ash content 10–20% higher than that of other biomass fuels, and more importantly, silicon dioxide therein accounts for 80% of the ash.[16] Rice husk MSNs (referred to as rMSNs hereafter) have a high specific surface area and retain all the advantages of traditional MSNs: (1) many ligands on their surface can be modified; (2) they have a large pore volume, thereby having a high drug-loading capacity; (3) they are not deposited in the body; (4) they are easily biodegraded; and (5) their main structure is silica oxide, the silanol group known to provide a better environment to protect drugs and modify the chemical surface.[17,18]

Based on these concepts, we report the synthesis of rMSNs with a dual-target function and triple therapy for cancer treatment. The design and synthetic strategy for rMSN-EuGd-Bi@CPT-HA-FA are illustrated in Scheme 1. FA and HA were attached to the rMSN surface functions as cell dual targets and gatekeepers, and then the anti-cancer drug camptothecin (CPT), the photosensitizer (Eu^{3+} ions), and photothermal materials (bismuth, Bi) were loaded into the pores of the rMSNs. Finally, we doped rMSNs with Gd^{3+} ions for magnetic resonance imaging (MRI). As a result, HAase decomposed HA-coated nanoparticles in the lysosome, releasing the anti-cancer drug CPT, and 808 nm light irradiation contributed to PDT and PTT. This study combines three therapies namely chemotherapeutics, PDT, and PTT with controlled release, enabling the material to simultaneously manifest the controlled release effect and increase the accumulation of drugs within cancer tissues. Finally, MRI was used to track the lesion location in clinical applications.

2. Materials and methods

2.1. Materials

(3-Aminopropyl)triethoxysilane (APTES, 98%) was purchased from ACROS. Europium(III) chloride hexahydrate ($EuCl_3 \cdot 6H_2O$, 99%), gadolinium(III) chloride hexahydrate ($GdCl_3 \cdot 6H_2O$, 99%), and 1-ethyl-3-(3-dimethylaminopropyl)carbodiimide (EDC, 98%) were purchased from Alfa Aesar. Dimethyl sulfoxide (DMSO, 40%), potassium phosphate monobasic (KH_2PO_4, 99%), sodium hydroxide (NaOH, 99%), sodium phosphate dibasic (Na_2HPO_4, 99%), and 99% toluene were purchased from J. T. Baker. Potassium chloride (KCl, 99%) was purchased from Mallinckrodt Chemicals. Tetraethyl orthosilicate (TEOS; 98%), hexadecyltrimethylammonium bromide (CTAB, 99%), 97% $Bi(NO_3)_3 \cdot 5H_2O$, 99% $NaBH_4$, polyvinylpyrrolidone (PVP) M.W. 58000, folic acid (FA, 98%), *N*-hydroxysuccinimide (NHS, 98%), camptothecin (CPT, 99%), hyaluronic acid sodium salt from *Streptococcus equi* (HA, mol wt: ~1.5–1.8 × 10^6 Da), (2-(*N*-morpholino)ethanesulfonic acid, 4-morpholineethanesulfonic acid) (MES), and sodium chloride (NaCl) were purchased from Sigma-Aldrich. Minimum essential media (MEM) was purchased from Biowest. Non-essential amino acids (NEAA), fetal bovine serum (FBS), antibiotic–antimycotic (AA), and trypsin were purchased from Gibco. Ethylenediaminetetraacetic acid (EDTA), thiazolyl blue tetrazolium bromide (MTT), formaldehyde, and Triton

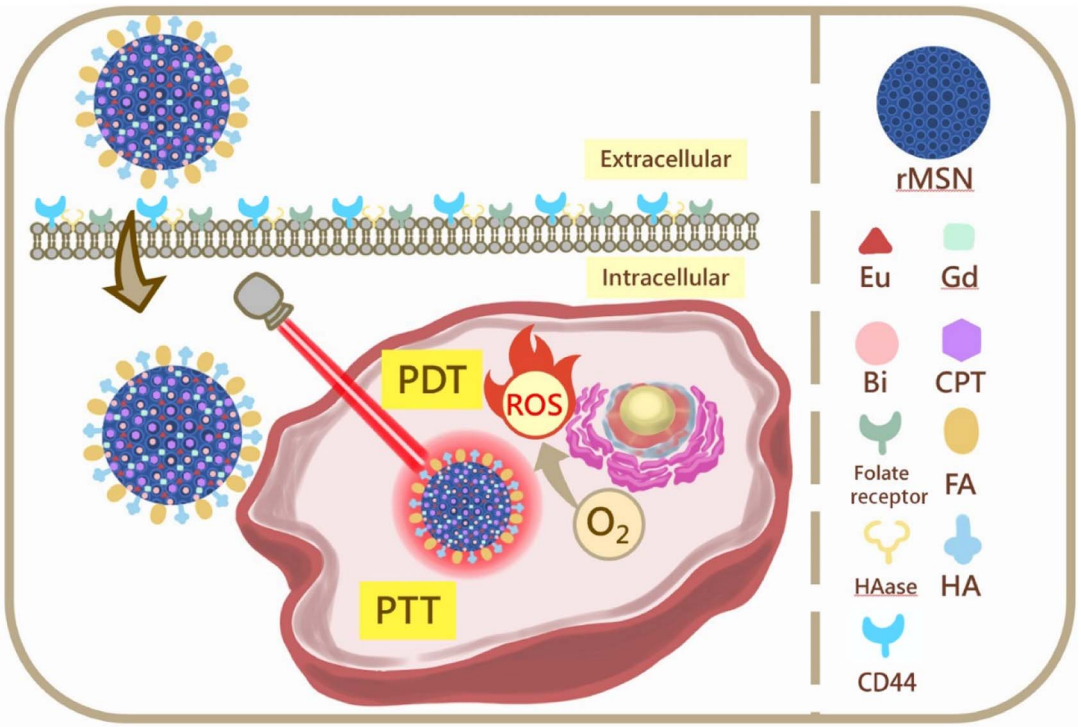

Scheme 1 Nanoparticles loaded with drugs (CPT). rMSN-EuGd-Bi@CPT-HA-FA enters the tumor cells by binding to the receptor (CD44) on the tumor cell and the target (FA and HA) and then use the triple combination therapy of anti-cancer drugs, PDT, and PTT to achieve good treatment efficiency.

X100 were purchased from Sigma-Aldrich. 4′,6-Diamidino-2-phenylindole (DAPI) Fluoromount-G was purchased from Southern Biotech. Rice husk purchased from HUALIEN CITY FARMER'S ASSOCIATION.

2.2. Biological silicon source-preparation steps of sodium silicate solution

First of all, placed 5.0 g the crushed rice husks, and added 50 mL 0.1 M HCl into a 100 mL round-bottomed flask, and the mixture was heated at 100 °C for 12 h in 360 rpm. Then, neutralize the sample by using deionized water, filtered solid product, and dried in a hot-air oven at 100 °C. Finally, calcined the dried product was at 700 °C for 4 h to ensure completely calcination, and get the silica dioxide. Mixed the 3.8 g silica dioxide powder with 1 g NaOH and 38.0 mL deionized water, refluxed at 100 °C overnight in 300 rpm, and filtered obtain the biological sodium silicate solution as previous work.[19]

2.3. Synthesis of MSN and rMSN-EuGd-Bi-NH_2

1 g of CTAB as surfactant and 1.4 mL 1 M NaOH mixed into 97 mL of deionized water, stirring and keep the solution at 80 °C until transparent. Then, 1 mL of 98% TEOS was added dropwise, stirred for 2 h, washed with water and ethanol three times, and fired to obtain MSN.[20] For rMSN-EuGd, replaced the TEOS with 3 mL of biological sodium silicate solution, and added 3 mL of 0.05 M $EuCl_3 \cdot 6H_2O$ (europium(III) chloride hexahydrate) and $GdCl_3 \cdot 6H_2O$ (gadolinium(III) chloride hexahydrate) stirred for 2 h. Then, washed the product three times with water, ethanol, methanol, and calcined 6 h at 650 °C.[21] Next, 30 mg of rMSN-EuGd was added to 15 mL of deionized water and stirred for 30 min. In addition, 300 mg of polyvinylpyrrolidone (PVP, M.W 58 000) and 100 mg of $Bi(NO_3)_3 \cdot 5H_2O$ were prepared in 10 mL of ethanol. The mixture was stirred at 55 °C for 30 min, then add the 10 mL 0.01 M $NaBH_4$ solution in EtOH to the precipitate, shake it for 1 min, centrifuge, and washing with deionized water several times. The sample was then vacuum dried at room temperature, and finally, the synthetic material rMSN-EuGd-Bi was obtained. To obtain rMSN-EuGd-Bi-NH_2, mixed 0.1 g of rMSN-EuGd-Bi and 0.2 mL of APTES in 15 mL toluene, and stirred 4 h at 120 °C, centrifuged, and washed by ethanol in twice.[20]

2.4. rMSN-EuGd-Bi-NH_2 loaded with CPT (rMSN-EuGd-Bi@CPT)

First, 10 mg CPT (camptothecin) and 50 mg of rMSN-EuGd-Bi-NH_2 mixed in 5 mL DMSO and vibrated ultrasonically for 1 h. Then, the mixture was stirred for 24 h and washed with deionized water several times. Most of the supernatant was removed using centrifugation and vacuum dried for 48 h before loading onto the CPT.

2.5. Synthesis of rMSN-EuGd-Bi@CPT-HA

10 mg of rMSN-EuGd-Bi@CPT-HA was dispersed in 10 mL of 0.01 M, pH 5.5 MES solution, then added 10 mg of HA, 10 mg of EDC, and 10 mg of NHS, and the mixture was stirred 12 h at room temperature. Removed the supernatant liquid by centrifugation and lyophilized overnight the precipitate to obtain the product.

2.6. Synthesis of rMSN-EuGd-Bi@CPT-HA-FA

First, 132 mg FA, 300 mg EDC, and 180 mg NHS were added to 20 mL of DMSO and stirred evenly for 4 h. Then, 200 mg of rMSN-EuGd-Bi@CPT-HA and 100 mL toluene were continuously stirred for 20 h. Then, the precipitate was obtained by centrifugation, washed with methanol several times, and finally dried in a vacuum overnight to obtain rMSN-EuGd-Bi@CPT-HA-FA.[22]

2.7. Characterization

For material analyses, using Bruker D2 phases for powder X-ray diffraction (XRD), using the Malvern Zetasizer Nano ZS system dynamic light scattering (DLS) to analyses the zeta potential and particle size. Transmission electron microscopy (TEM) images, and energy dispersive spectra (EDS) were obtained by Tecnai F30 instrument that used applied voltage in 300 kV. Scanning electron microscopy (SEM) was obtain by Hitachi S-3400N that used applied voltage in 30 kV, working distance about 35 mm, and SE detector. Using ASAP 2020 Micromeritics for nitrogen adsorption isotherms Barrett–Joyner–Halenda (BJH) analysis, surface area and pore size distribution curves of doped or undoped nanoparticles were using the Brunauer–Emmett–Teller (BET) method. T_1-weighted MR imaging was performed using a 7 T scanner (BRUKER S300 BIOSPEC/MEDSPEC MRI, Karlsruhe, Germany) with conventional spin-echo acquisition (TR/TE = 300 ms/10.6 ms, slice thickness = 2.00 mm). The concentrations of Eu^{3+} and Gd^{3+} ions doped into nanoparticles were measured by inductively coupled plasma mass spectrometry (ICP-MS). Using a Jasco FP-6300 photoluminescence spectrometer with an ex = 395 nm to recorded luminescence excitation spectra. Using a BRUKER TENSOR Series II spectrometer identified the surface functionalized rMSNs molecular Fourier transform infrared (FTIR) spectra. Thermogravimetric analysis (TGA) curves were obtained using a Netzsch TG 209 F3 instrument to determine the binding efficiency of HA when the temperature was increased to 700 °C, rate of temperature elevation: 10.00 K min^{-1}. Using the oven (Lindberg Blue/M Deluxe 300 °C Mechanical Convection Oven controller UP-150) for calcination of samples at the heating rate of 1 °C per min. For synthetic experiments, the magnetic stirrer (CORNING PC-420D) will be used for stirring, the centrifuge (KUBOTA 5910) for centrifugation, and the lyophilizer (BOYIKANG FD-1C-50) for lyophilization.

2.8. Drug release

First, 5 mg of rMSN-EuGd-Bi@CPT and rMSN-EuGd-Bi@CPT-HA were added to 3 mL of dimethyl sulfoxide (DMSO) and shaken evenly. Then, measured the 480 nm wavelength absorbance value at 0, 10, 20, 30, 40, 50, 60, 80, 100, 120, 150, 180, 210, 240, 270, 300, 360, 420, and 480 min. Total drug release dose was calculated by adding the concentration calibration curve of the absorbance value at 480 nm, previously read.

2.9. Photothermal experiment

Prepared different concentration of rMSN-EuGd-Bi (0, 100, 200, 400 g mL^{-1}) by using phosphate-buffered saline (PBS), irradiate the solution by light source (1 W cm^{-2}) containing 808 nm wavelength and recorded the temperature every 30 s until stabilized, then stop the irradiation, and the temperature was recorded every 30 s till room temperature.

2.9.1 PBS buffer preparation method. Weight 0.20 g KCl, 1.44 g Na_2HPO_4, 8.00 g NaCl, and 0.24 g KH_2PO_4 dissolve in 800 mL distilled water, and using HCl adjust to pH 7.4 and finally add distilled water to 1 L to obtain a PBS buffer.

2.10. Photodynamic experiment-reactive oxygen species assay (DPBF experiment)

Prepared 5 mL ethanol that contain 0.1 g rMSN-EuGd or rMSN-EuGd-Bi and 0.08 M DPBF, then irradiated with containing 808 nm wavelength light source (1 W cm^{-2}) and recorded the 410 nm absorbance after 1, 3, 5, 10 and 15 min irradiation by using ELISA reader. This experiment avoid light except irradiation.

2.11. *In vitro* experiments

2.11.1. Cell culture. L929 cells (*Mus musculus* fibroblast cell line) and A549 cells (adenocarcinomic human alveolar basal epithelial cells) were cultured in MEM and F12K supplemented with 10% FBS and 1% antibiotics (AA) at 37 °C in an environment containing 5% CO_2.

2.11.2 Cell viability assay. The L929 cells were used as a normal cell model, and A549 cells were used as a cancer cell model for the control and experimental conditions, respectively. The experimental steps were as follows:

First, seeded 1×10^4 cells per well in 96-well and incubated for 24 h at 37 °C. Next, co-culture with different concentration (25, 50, 100, 200 μg mL^{-1}) drug carrier per well for 6 h. Remove the medium, wash twice by PBS, added fresh medium and irradiated light source (1 W cm^{-2}) containing 808 nm wavelength for 15 min. Later, added 20 μL of MTT to each well reaction 4 h. Used 100 μL DMSO and shaken 15 min to dissolve formazan, reading the Optical Density (OD) value 540 nm using an enzyme immunoassay analyzer (ELISA reader). The cell viability rate was calculated as:

$$\text{Cell viability} = \frac{OD_{540}\ (\text{test group})}{OD_{540}\ (\text{control group})} \times 100\%$$

2.11.3 Confocal image analysis. First, placed the sterilized 13 mm glass coverslip in 24-well, then seeded 2×10^4 cells per well and cultured for 24 h. Next, cultured with 100 μg mL^{-1} medium/material mixture 500 μL for 6 h. Cultures were then

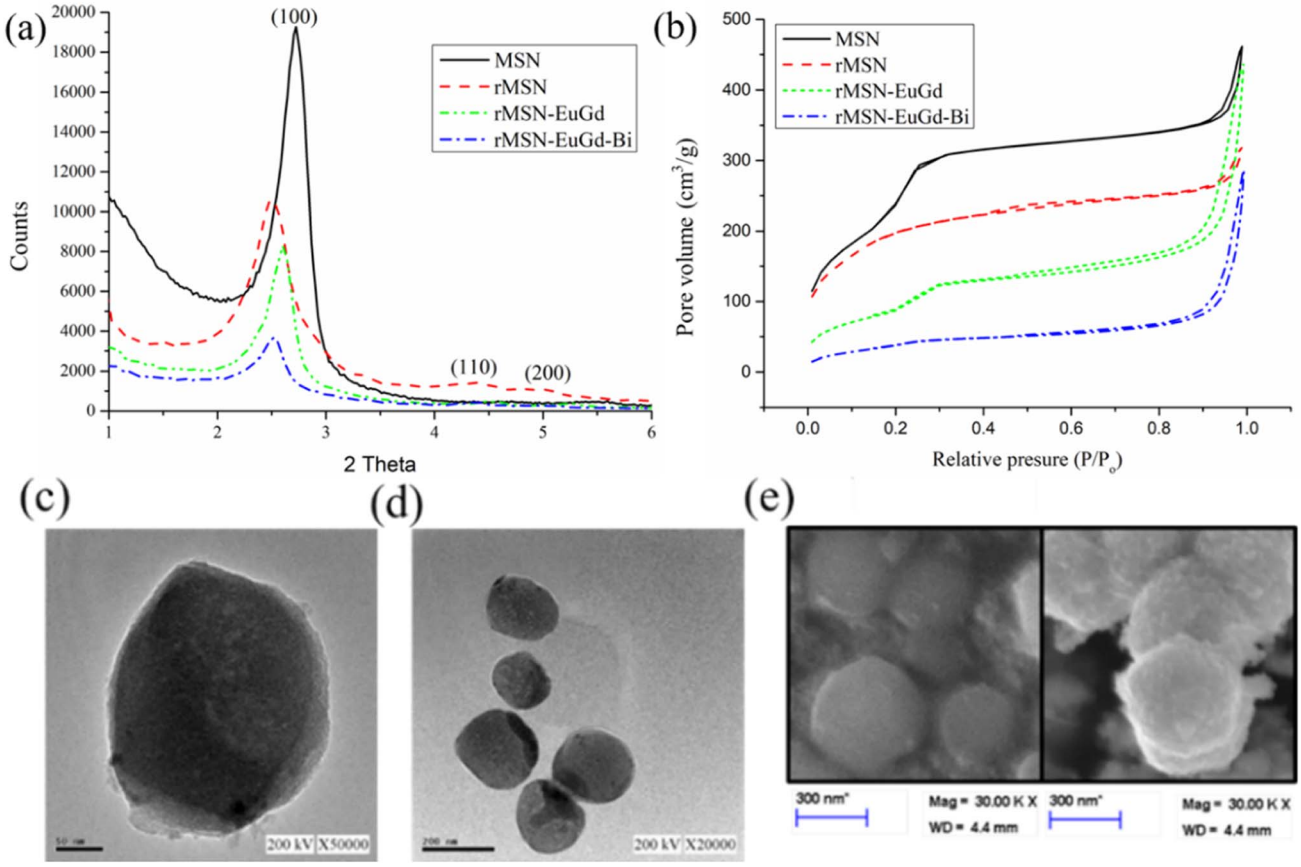

Fig. 1 (a) Small angle XRD analysis of MSN, rMSN, rMSN-EuGd, and rMSN-EuGd-Bi, (b) isothermal nitrogen adsorption of rMSN-EuGd and rMSN-EuGd-Bi, (c and d) analysis of rMSN-EuGd structure and size using TEM. Scale bar: (c) 50 nm, (d) 0.2 μm. (e) The scanning electron microscope (SEM) images of rMSN-EuGd and rMSN-EuGd-Bi showing particle size and morphology.

washed with PBS, 300 μl of 3.7% formaldehyde/PBS solution was added for 10 min for fixation, and a 5 min incubation with DAPI was used to stain nuclei. Finally, washing with PBS, mounted the coverslip onto a glass slide and phagocytosis of the cells and materials was observed using confocal laser scanning microscopy (CLSM).

3. Results and discussion

3.1. Structure, formation, morphology, and properties of rMSN-EuGd and rMSN-EuGd-Bi

As Fig. 1a shown, the results of small-angle powder X-ray diffraction (XRD) analyzes of MSN, rMSN, rMSN-EuGd, and rMSN-EuGd-Bi show sharp diffraction peaks in the (100), (110), and (200) lattice directions and are regularly distributed, represented that the materials have regularly hexagonal mesoporous structure. The hexagonal but mesoporous structure of the material was unaffected by the incorporation of Eu and Gd.[23] Therefore, the nanoparticle carrier rMSN, which is prepared from rice husks and used for the synthesis of biosilicon, has the same structure as the nanoparticle carrier rMSN synthesized using chemicals. It had a hexagonal and regular arrangement of pores. The rMSN synthesized from biological silicon sources *d*-spacing was calculated by the XRD pattern to be 3.56 nm, and the MSN synthesized from chemical silicon source was 3.29 nm, the rMSN-EuGd synthesized by using biological silicon source and doped with europium (Eu) and gadolinium (Gd) was 3.47 nm, and the rMSN-EuGd-Bi was 3.39 nm, as Table 1 show. The above results show that the pore structure of the nanoparticle carrier is slightly changed by doping with metal ions, but it does not affect its overall main structure. The experiment used BET analysis of MSN, rMSN, rMSN-EuGd and rMSN-EuGd-Bi was performed. Fig. 1b shows that the nitrogen constant temperature adsorption and the pore

Table 1 BET and PXRD analyses of the properties of MSN-EuGd

Physical data	Units	MSN	rMSN	rMSN-EuGd	rMSN-EuGd-Bi
BET surface area	$m^2\ g^{-1}$	788.74	666.03	680.41	263.31
Pore volume	$cm^3\ g^{-1}$	0.84	0.36	0.63	0.39
BJH desorption diameter	nm	3.38	3.53	2.49	2.32
XRD 2θ	°	2.64	2.34	2.53	2.60
d Spacing	nm	3.34	3.77	3.47	3.39
Wall thickness	nm	0.48	0.82	1.52	1.59

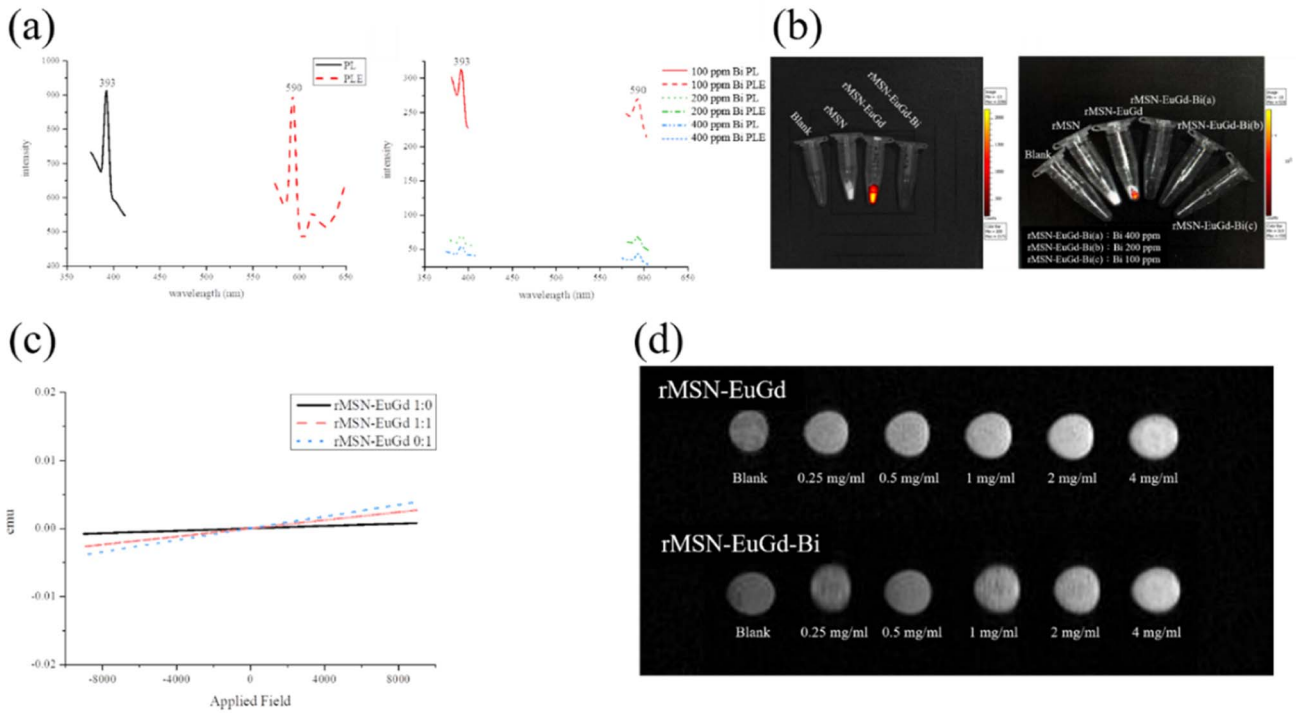

Fig. 2 (a) PLE and PL results showing emission spectra of the rMSN-EuGd-Bi with different density Bi. (b) IVIS optical imaging of blank, rMSN, rMSN-EuGd, and rMSN-EuGd-Bi with different density Bi. (c) The magnetic properties of rMSN-EuGd measured by a superconducting quantum interference device (SQUID) magnetometer. (d) T_1-weighted MRI of rMSN-EuGd and rMSN-EuGd-Bi with different density (0.25–4 mg mL^{-1}). As the concentration of the material increases, the brightness increases as a result of the magnetic development performance.

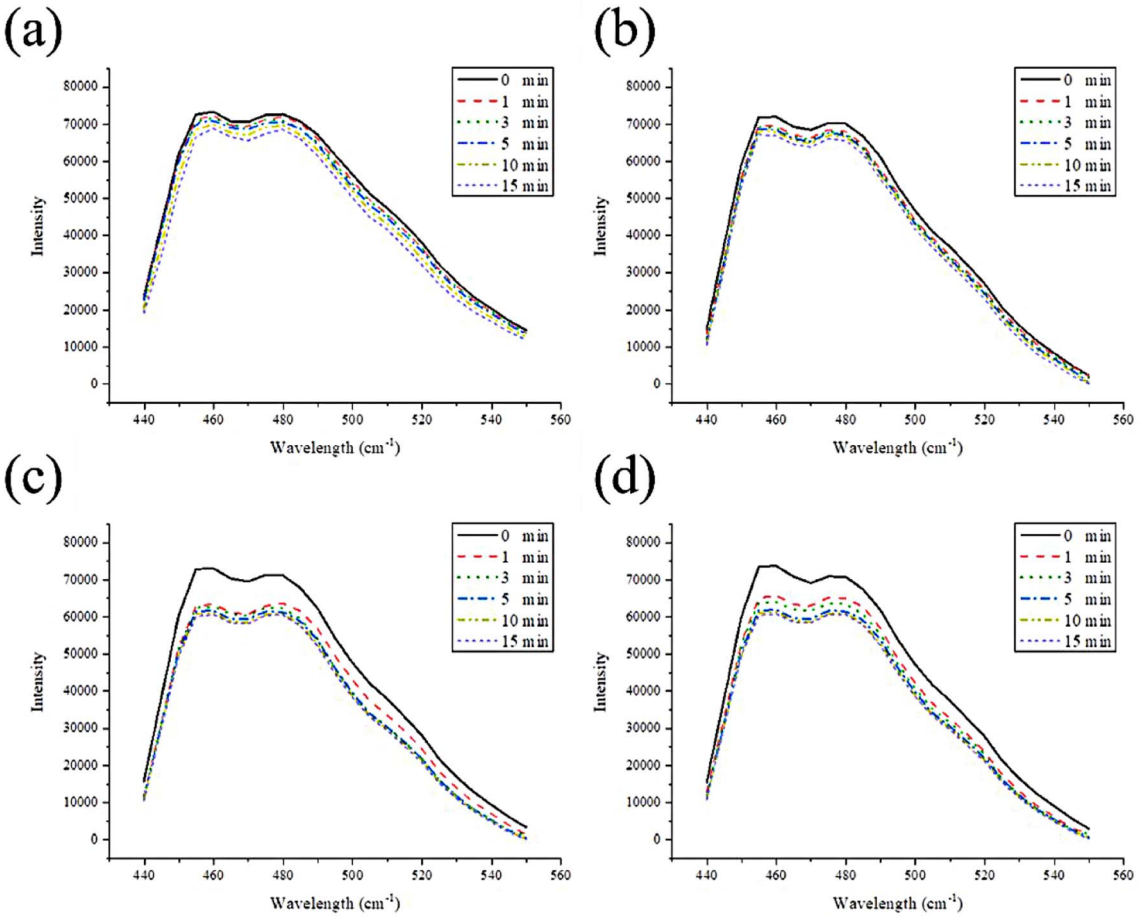

Fig. 3 Photodecomposition of DPBF by $^1O_2$ after irradiation (a) blank, (b) rMSN, (c) rMSN-EuGd, and (d) rMSN-EuGd-Bi.

size distribution curve of MSN, rMSN, rMSN-EuGd and rMSN-EuGd-Bi were of type IV, which indicates a mesoporous structure determined by a hysteresis loop.[24] The pore diameter of rMSN-EuGd was 2.49 nm, the specific surface area was 680.41 $m^2\ g^{-1}$, and the pore volume was 0.63 $cm^3\ g^{-1}$. The pore diameter of rMSN-EuGd-Bi was 2.32 nm, specific surface area was 263.31 $m^2\ g^{-1}$, and pore volume was 0.39 $cm^3\ g^{-1}$ in Table 1. The structure and size were observed using TEM and scanning electron microscopy (SEM) analyses. rMSN-EuGd and rMSN-EuGd-Bi had a regular hexagonal pore structure, and each particle had a uniform size.[25] Fig. 1c shows that the measured data were consistent; the particle size of rMSN-EuGd was approximately 200–300 nm, and the particle size of rMSN-EuGd-Bi was approximately 250–350 nm. EDS can be used to determine the elements present in a material. Fig. S2† demonstrates that elements such as silicon (Si), oxygen (O), Bi, Eu, and Gd were detected in rMSN-EuGd-Bi and rMSN-EuGd containing Si, O, Eu, and Gd, whereas rMSN contained only Si and (O, which were further quantified by inductively coupled plasma mass spectrometry (ICP-MS) to obtain Eu and Gd contents, respectively, as shown in Table S1.†

Used PL spectroscopy to demonstrate the imaging capabilities of rMSN-EuGd-Bi. It was excited by a light source with a wavelength of 395 nm, generating radiative absorption peaks at 590 nm and 615 nm, centered on the red emission peaks of Eu^{3+} at $^5D_0 \rightarrow {}^7F_1$ (590 nm) and $^5D_0 \rightarrow {}^7F_2$ (615 nm), receive excitation light,[26] as shown in Fig. 2a. In addition, the experimental results also showed that rMSN-EuGd-Bi may be due to

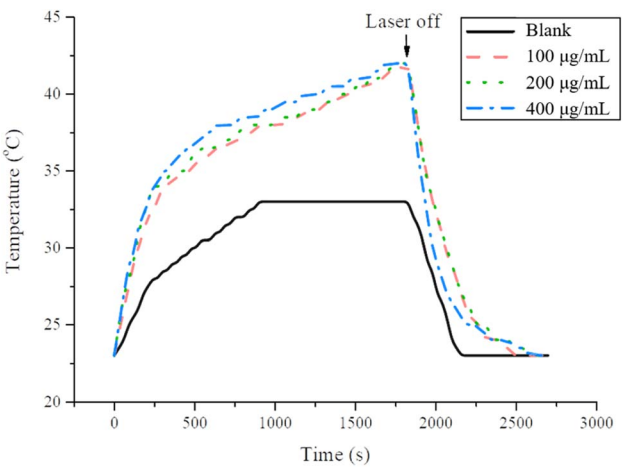

Fig. 4 The photothermal response of rMSN-EuGd-Bi in PBS solution for 1800 s with 808 nm laser. Recorded temperature changed every 30 s until the temperature stabilized.

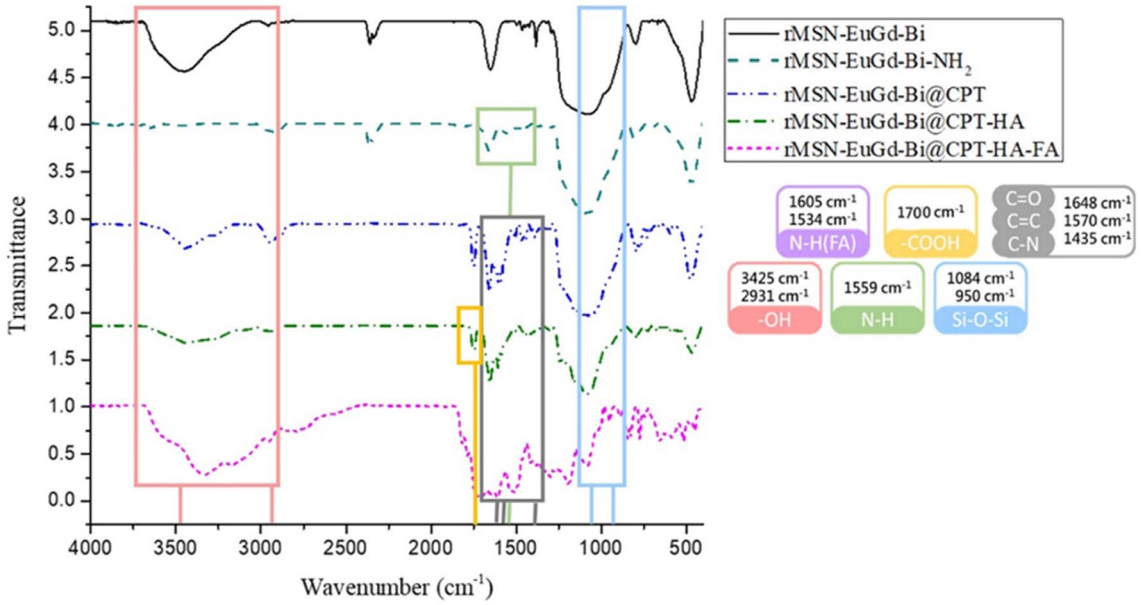

Fig. 5 FTIR analysis spectra of rMSN-EuGd-Bi, rMSN-EuGd-Bi-NH2, rMSN-EuGd-Bi, rMSN-EuGd-Bi@CPT, rMSN-EuGd-Bi@CPT-HA, and rMSN-EuGd-Bi@CPT-HA-FA.

Bi, so an obvious Eu fluorescence signal could not be observed under IVIS irradiation with an excitation wavelength of 430 nm. It is speculated that the fluorescence signal of Eu absorbs 395 red light emitted after light with a wavelength of nm, so ultraviolet light is used to prove its luminescence characteristics. Under irradiation at an excitation wavelength of 254 nm, a weak red fluorescence signal of Eu was observed (Fig. S3†); when the wavelength was 254 nm when irradiated with ultraviolet light, the Eu in rMSN-EuGd and rMSN-EuGd-Bi was excited by ultraviolet light and emitted a red fluorescent signal, whereas rMSN was not doped with Eu, so it was not affected by ultraviolet light. Fluorescent development characteristics are shown. IVIS was used to illuminate rMSN, rMSN-EuGd, and rMSN-EuGd-Bi at an excitation wavelength of 430 nm. As shown in Fig. 2b, rMSNs and a blank were observed to have no obvious fluorescence characteristics, whereas rMSN-EuGd showed very obvious fluorescence excitation, confirming that IVIS can effectively detect the materials.

To investigate the magnetic properties of the material, we synthesized rMSN-EuGd with various lanthanide ratios and

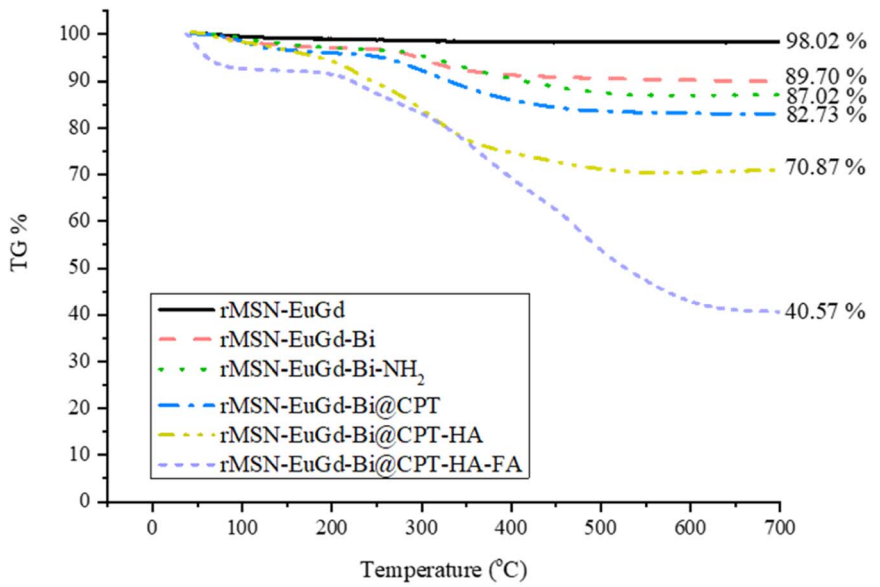

Fig. 6 Thermogravimetric analysis (TGA) weight loss curves of rMSN-EuGd-Bi, rMSN-EuGd-Bi-NH_2, rMSN-EuGd-Bi, rMSN-EuGd-Bi@CPT, rMSN-EuGd-Bi@CPT-HA, and rMSN-EuGd-Bi@CPT-HA-FA.

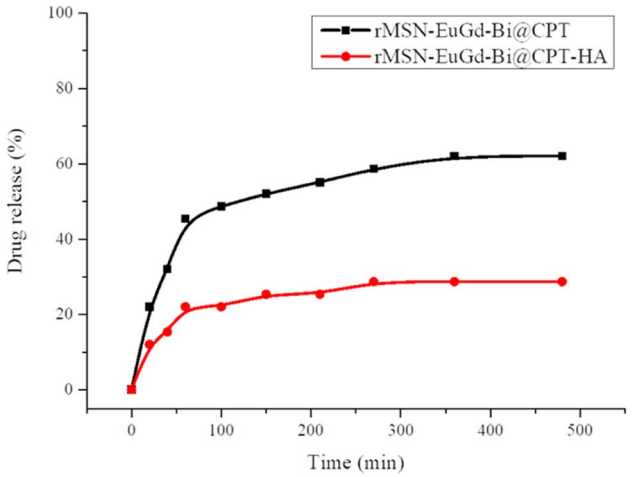

Fig. 7 Drug release of rMSN-EuGd-Bi@CPT and rMSN-EuGd-Bi@CPT-HA in dimethyl sulfoxide (DMSO).

measured the results in a superconducting quantum interference device. The undoped Gd^{3+} material showed no magnetic properties, while the Gd^{3+} doped MSNs exhibited paramagnetic phenomena. As the Gd^{3+} concentration increased, the paramagnetic properties became more pronounced, confirming that the material was paramagnetic as Fig. 2c shown. MR imaging was also applied to rMSN-EuGd and rMSN-EuGd-Bi to perform *in vitro* MRI tests. From Fig. 2d, it can be confirmed that the T_1 weight image becomes brighter with increasing material concentration, and rMSN-EuGd-Bi can be used as a positive T_1 developed image.[27]

To verify that MSN-EuGd can indeed generate active oxygen through illumination, a DPBF experiment was performed, as required for PDT. As shown in Fig. 3, after comparison, the analysis results of blank and rMSN for the group with no added material showed almost no difference in fluorescence signal intensity after 15 min of light, whereas rMSN-EuGd and rMSN-EuGd-Bi showed fluorescence signals. Poor strength (approximately 9000–12 000 intensity) results in material properties that can be used in PDT. This phenomenon confirms that the ROS generated by light of appropriate wavelength after doping with lanthanide metal ions greatly reduces the fluorescence intensity of DPBF[28] and confirming that the material has the properties of PDT. Different concentrations of rMSN-EuGd-Bi were irradiated for 1800 s using the 808 nm wavelength light source until the temperature stabilized, then the light source was turned off and the temperature changes were recorded every 30 s. According to the results of Fig. 4, different concentrations of rMSN-EuGd-Bi can reach 42 °C to achieve the effect of PTT.[29]

According to dynamic light scattering (DLS) analysis, the size of organic molecules can change while being grafted onto the material. The size of the first nanoparticle rMSN-EuGd was 248.8 nm and the surface charge was −29.5 mV; after the synthesis of rMSN-EuGd-Bi, the size became 268.2 nm, and the surface charge of the Bi metal increased to −13.8 mV.[30] When the amino group ($-NH_2$) is connected, the size becomes 296.3 nm and positively charged to increase the surface charge to −8.06 mV,[31] and after the first active target HA is connected, the nanoparticle size becomes 343.6 nm. Because HA has negatively charged –COOH, the detected surface charge is −13.3 mV.[32] Finally, after the second active target FA is connected, the nanoparticle size increased to 350.5 nm, because FA is a positively charged $-NH_2$ group, so the surface charge detected after the dual target is finally connected is 12 mV in Table S2.†

To confirm whether the organic molecules were successfully conjugated to rMSN-EuGd-Bi, we analyzed the functional groups of the material as Fig. 5 shown. –OH groups were

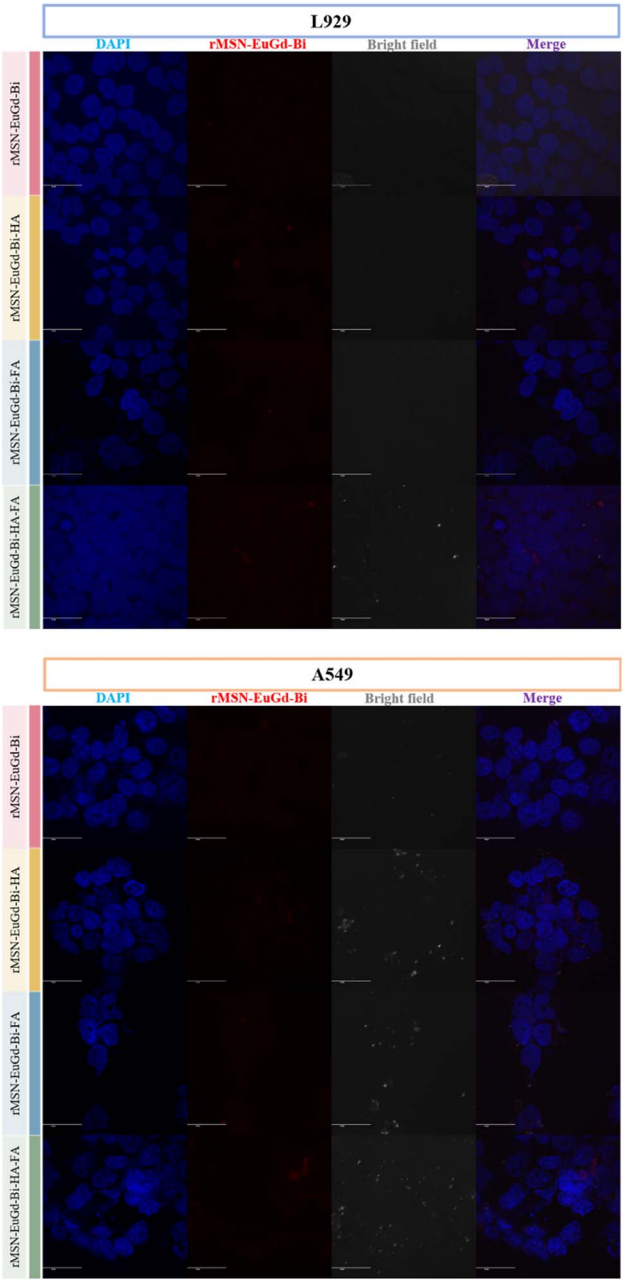

Fig. 8 *In vitro* selective anticancer effects and mechanisms of the nanoparticle drug delivery system. Confocal images of treated L929 and A549 cells where nuclei and nanoparticles were stained blue and red, respectively.

observed at 3425 cm^{-1} and 2931 cm^{-1} and Si–O–Si signals were observed at 1084 cm^{-1} and 950 cm^{-1}.[33] The addition of the –NH_2 group confirmed an additional N–H bond peak at the amine group observed at 1559;[34] after loading the drug molecule CPT, it was found that there were C=O bonds, C=C bonds, and C–N bonds at 1648 cm^{-1}, 1570 cm^{-1}, and 1435 cm^{-1}, respectively, confirming the existence of the drug[35] After the HA target, the carboxylic acid (–COOH) group was found at 1700 cm^{-1};[36] after the FA target with the N–H functional group was finally attached, the N–H characteristic peaks appeared at 1605 cm^{-1} and 1534 cm^{-1},[37] and the FT-IR spectrum indicated that the prepared material molecules were successfully connected to rMSN-EuGd-Bi.

TGA was used to determine the amount and drug loading capacity of rMSN-EuGd-Bi modified with organic molecules. In this experiment, the temperature of each material was increased from 40 °C to 700 °C in a pure oxygen environment and the weight loss rate of each material was observed. The amount of each molecule connected to rMSN-EuGd-Bi is listed in Table S3.† The –NH_2 modification was 34.69 mg g^{-1}, followed by an amount of CPT of approximately 55.53 mg g^{-1}, amount of HA of approximately 135.53 mg g^{-1} and a final amount of FA of approximately 393.50 mg g^{-1} as Fig. 6 shown.

To confirm drug release, rMSN-EuGd-Bi@CPT and rMSN-EuGd-Bi@CPT-HA were added to the dimethyl sulfoxide (DMSO), as the results of Fig. 7, and rMSN-EuGd-Bi@CPT-HA was approximately 60% and the rMSN-EuGd-Bi@CPT-HA was approximately 23%.

3.2. *In vitro* cytotoxicity and cellular uptake of functionalized rMSN-EuGd-Bi

To confirm phagocytosis by cells for each material, mouse fibroblasts (L929) were compared with human lung adenocarcinoma cells (A549) as a CD44 receptor and folate receptor control group, and CLSM images were taken after 6 h of co-culture with each material. As shown in Fig. 8, bare rMSN-EuGd-Bi was hardly phagocytized by L929 and A549 cells, and the A549 cells were able to phagocytose more rMSN-EuGd-Bi-HA and rMSN-EuGd-Bi-FA than L929 cells. It is speculated that overexpression of CD44 and folate receptors in A549 cells enables the entry of rMSN-EuGd-Bi-HA or rMSN-EuGd-Bi-FA

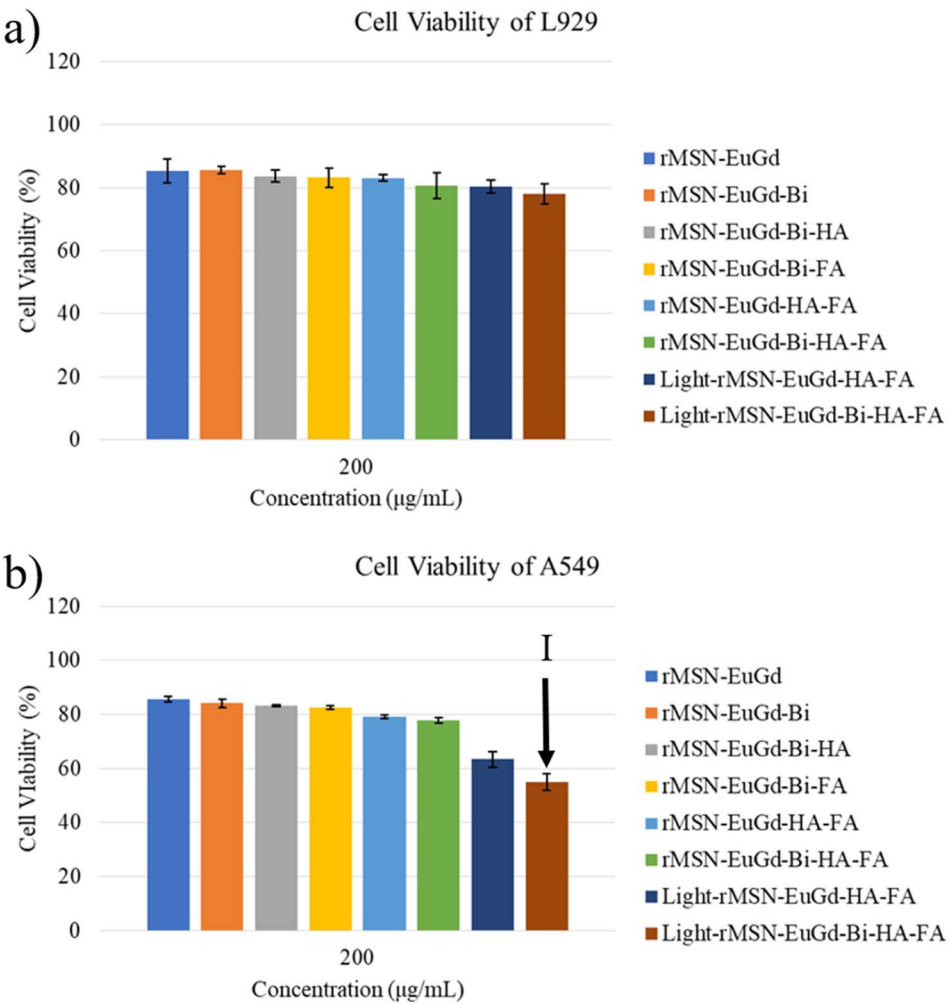

Fig. 9 MTT assays of 200 μg mL^{-1} rMSN-EuGd, rMSN-EuGd-Bi, rMSN-EuGd-Bi-HA, rMSN-EuGd-Bi-FA, rMSN-EuGd-HA-FA, rMSN-EuGd-Bi-HA-FA, light-rMSN-EuGd-HA-FA, and light-rMSN-EuGd-Bi-HA-FA (lighting condition: 808 nm irradiation for 15 min) to (a) L929 cell, (b) A549 cell (state I: dual-targeting + PDT).

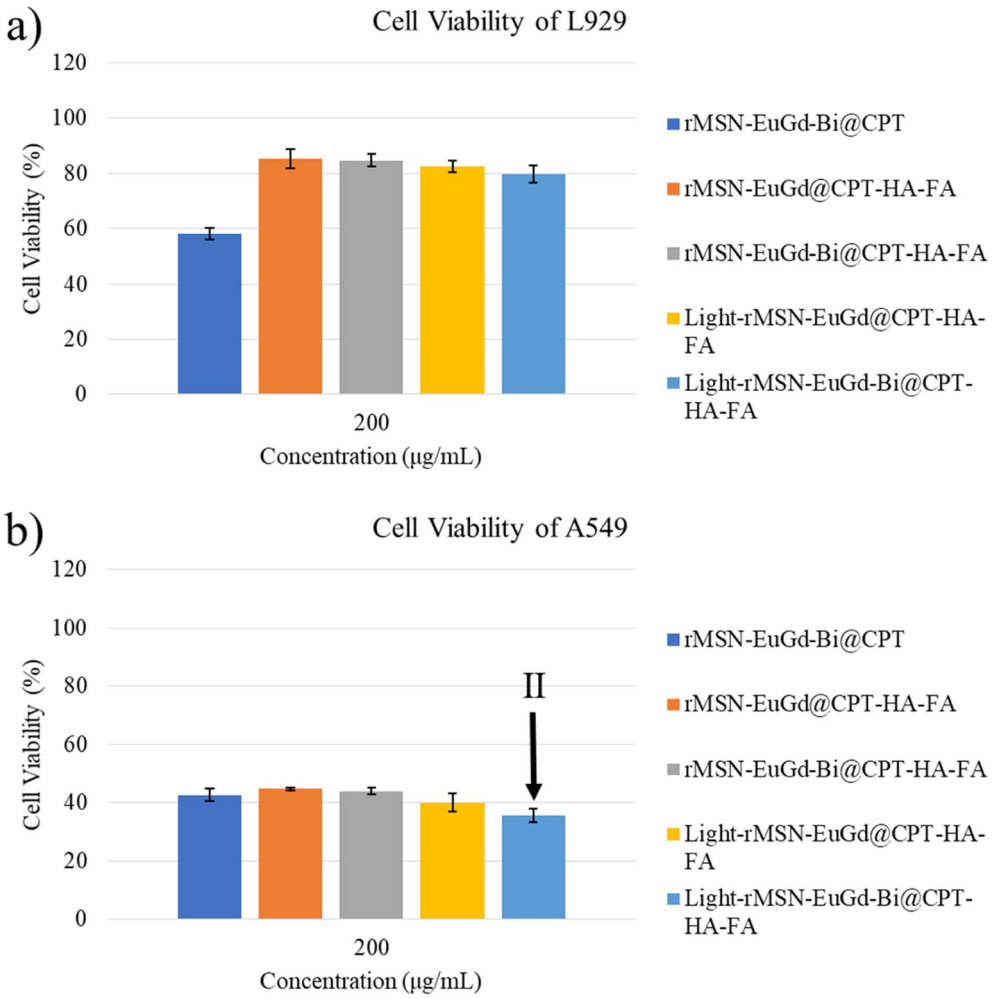

Fig. 10 MTT assays of 200 μg mL^{-1} rMSN-EuGd-Bi@CPT, rMSN-EuGd@CPT-HA-FA, rMSN-EuGd-Bi@CPT-HA-FA, light-rMSN-EuGd@CPT-HA-FA, and light-rMSN-EuGd-Bi@CPT-HA-FA (lighting condition: 808 nm irradiation for 15 min) to (a) L929 cell, (b) A549 cell (state II: dual-targeting + CPT and PDT).

into cells by receptor endocytosis, suggesting that the material is cancer. It suggests that it may be selectively taken up by cells and enter cancer cells. Furthermore, the signal intensities of confocal images of A549 cells in the presence of rMSN-EuGd-Bi-HA-FA increased dramatically, which supports the idea that the presence of dual-targeted groups on rMSN is sufficient for active targeting of cancer cells.

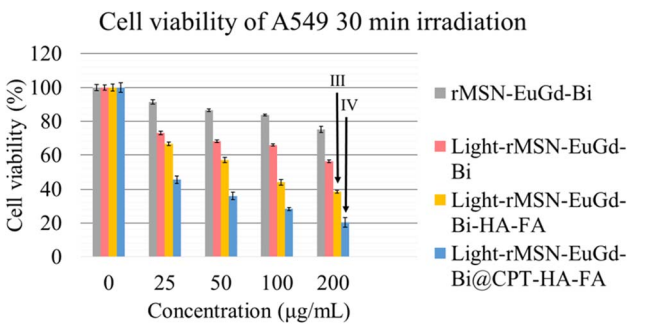

Fig. 11 MTT assays for rMSN-EuGd-Bi, light-rMSN-EuGd-Bi, light-rMSN-EuGd-Bi-HA-FA, and light-rMSN-EuGd-Bi@CPT-HA-FA (lighting condition: 808 nm irradiation for 30 min) to A549 cells (state III: dual targeting + PTT and PDT; state IV: dual targeting + PTT, PDT, and CPT).

The viability of A549 and L929 normal cells was assessed using the MTT assay to investigate the cytotoxicity of these rMSN. Cell viability testing confirmed that these rMSN materials were cytotoxic to cancer cells and were less harmful to normal cells (as Fig. 9, 10, S4 and S5†). As shown in Fig. 6a and S7a,† the viability of the L929 cells upon the addition of various amounts of these rMSN materials showed about 80% or more, indicating that these rMSN materials were not cytotoxic. It should be noted that the viability of the L929 cells with 200 μg mL^{-1} rMSN-EuGd-Bi-HA-FA remained approximately 80% under 808 nm irradiation for 15 min as Fig. 6a results. However, the viability of the A549 cells with 200 μg mL^{-1} light-rMSN-EuGd-Bi-HA-FA was lower than 60% as Fig. 6b shown, suggesting that dual-targeting and only PDT effects (state I).

Next, the viability of the L929 cells after the addition of various amounts of these rMSN loaded CPT materials remained

above 80%, except for the rMSN-EuGd-Bi@CPT because of none HA as the gatekeeper as Fig. 7a and S8a† present. In contrast, the viability of A549 cells decreased as the rMSN loaded CPT materials increased as results of Fig. 7b and S8b.† It was further noted that the viability of A549 cells with rMSN-EuGd-Bi@CPT-HA-FA showed only 35% under 808 nm irradiation for 15 min as Fig. 7b shown, which may be attributed to multiple functions including dual-targeting, CPT, and PDT (state II).

To achieve effective PTT, rMSN-EuGd-Bi@CPT-HA-FA must be irradiated for 30 min to allow the temperature to increase to 42 °C as Fig. 4 shown. Therefore, the viability of A549 cells with 200 μg mL^{-1} of rMSN-EuGd-Bi-HA-FA was lower than 40% under 808 nm irradiation for 30 min as result of Fig. 11, because of synergistic therapy of PTT, PDT, and the dual-target function (state III: dual-targeting, PTT, and PDT). Furthermore, the viability of A549 cells with 200 μg mL^{-1} of rMSN-EuGd-Bi@CPT-HA-FA displayed as low as 20% under 808 nm irradiation for 30 min, demonstrating the benefits of dual-targeted and triple-combination therapy (state IV: dual-targeting, PTT, PDT, and CPT). Based on the experimental results, the combined synergistic therapeutic effect in A549 cancer cells is more significant, and rMSN-EuGd-Bi@CPT-HA-FA is a promising new approach to cancer therapy.

4. Conclusion

In this study, we successfully used rice husks as a biological silica source and doped Eu^{3+} and Gd^{3+} for the photodynamic and magnetic resonance functions to synthesize rMSN-EuGd. Then, Bi nanoparticles and CPT were loaded into rMSN-EuGd for use as photothermal and chemotherapeutic agents, modified FA and HA on the nanoparticle surface for dual-targeting functions, and HA also acted as the drug gatekeeper. As a result of the drug release experiment, CPT was easily released when HAase appeared in the environment. In addition, confocal microscopy showed that FA and HA can target A549 cells by overexpressing the folate receptor and CD44. Finally, the viability of A549 cells co-cultured with 200 μg mL^{-1} of rMSN-EuGd-Bi@CPT-HA-FA showed only 20% under 808 nm irradiation for 30 min. This result testifies to efficacy of the dual-targeting and combinations of PTT, PDT, and chemotherapeutic. We hope that rMSN-EuGd-Bi@CPT-HA-FA is a new treatment method with full potential and vision.

Conflicts of interest

There are no conflicts to declare.

Acknowledgements

The authors are grateful to the National Science Council MOST 102-2113-M-019002, 103-2113-M-019-001-, 104-2113-M-019-002-, 105-2119-M-019-002-, 106-2113-M-019-003-, 107-2113-M-019-001-, MOST-110-2113-M-019-003-MY2, National Taiwan Ocean University, Center of Excellence for the Ocean, Center of Excellence for Ocean Engineering, and Taiwan International Algae Research Fund of National Taiwan Ocean University for financial support. We thank Instrumentation Center of National Tsing Hua University for technical support, ICP-MS.

References

1 K. D. Miller, *et al.*, Cancer treatment and survivorship statistics, *Ca-Cancer J. Clin.*, 2016, **66**(4), 271–289.
2 Y. J. Zhang, *et al.*, Risk factors and socio-economic burden in pancreatic ductal adenocarcinoma operation: a machine learning based analysis, *BMC Cancer*, 2020, **20**(1), 1161.
3 J. H. Byun and I. H. Jung, Phase-specific cancer-immune model considering acquired resistance to therapeutic agents, *Appl. Math. Comput.*, 2021, **391**, 125555.
4 M. E. B. Powell, Modern Radiotherapy and Cervical Cancer, *Int. J. Gynecol. Cancer*, 2010, **20**, S49–S51.
5 J. C. Yan, *et al.*, Aptamer-Targeted Photodynamic Platforms for Tumor Therapy, *ACS Appl. Mater. Interfaces*, 2021, **13**(24), 27749–27773.
6 C. X. Wei, *et al.*, Carbon spheres with high photothermal conversion efficiency for photothermal therapy of tumor, *Diamond Relat. Mater.*, 2022, **126**, 109048.
7 K. Nejati, *et al.*, Nanoparticle-based drug delivery systems to overcome gastric cancer drug resistance, *J. Drug Delivery Sci. Technol.*, 2022, **70**, 103231.
8 W. Lee, *et al.*, Europium-Diethylenetriaminepentaacetic Acid Loaded Radioluminescence Liposome Nanoplatform for Effective Radioisotope-Mediated Photodynamic Therapy, *ACS Nano*, 2020, **14**(10), 13004–13015.
9 Y. You, *et al.*, Photothermal Killing of A549 Cells and Autophagy Induction by Bismuth Selenide Particles, *Materials*, 2021, **14**(12), 3373.
10 Z. Y. Gong, *et al.*, Enzyme-Induced Transformable Peptide Nanocarriers with Enhanced Drug Permeability and Retention to Improve Tumor Nanotherapy Efficacy, *ACS Appl. Mater. Interfaces*, 2021, **13**(47), 55913–55927.
11 M. Y. Li, *et al.*, Controlling Conjugated Antibodies at the Molecular Level for Active Targeting Nanoparticles toward HER2-Positive Cancer Cells, *Mol. Pharm.*, 2021, **18**(3), 1196–1207.
12 Z. C. Deng, *et al.*, Dual Targeting with Cell Surface Electrical Charge and Folic Acid *via* Superparamagnetic Fe_3O_4@$Cu_{2-x}S$ for Photothermal Cancer Cell Killing, *Cancers*, 2021, **13**(21), 5275.
13 E. Chiesa, *et al.*, CD44-Targeted Carriers: The Role of Molecular Weight of Hyaluronic Acid in the Uptake of Hyaluronic Acid-Based Nanoparticles, *Pharmaceuticals*, 2022, **15**(1), 103.
14 Y. M. Zhou, *et al.*, Hyaluronic Acid-Functionalized Hollow Mesoporous Silica Nanoparticles as pH-Sensitive Nanocarriers for Cancer Chemo-Photodynamic Therapy, *Langmuir*, 2021, **37**(8), 2619–2628.
15 Z. Y. Wu, C. C. Lee and H. I. Lin, Hyaluronidase-Responsive Mesoporous Silica Nanoparticles with Dual-Imaging and Dual-Target Function, *Cancers*, 2019, **11**(5), 697.
16 S. Sankar, *et al.*, Biogenerated silica nanoparticles synthesized from sticky, red, and brown rice husk ashes by a chemical method, *Ceram. Int.*, 2016, **42**(4), 4875–4885.

17 S. Porrang, *et al.*, Preparation and *in vitro* evaluation of mesoporous biogenic silica nanoparticles obtained from rice and wheat husk as a biocompatible carrier for anti-cancer drug delivery, *Eur. J. Pharm. Sci.*, 2021, **163**, 105866.
18 Y. Yu, *et al.*, Short-Term Oral Administration of Mesoporous Silica Nanoparticles Potentially Induced Colon Inflammation in Rats Through Alteration of Gut Microbiota, *Int. J. Nanomed.*, 2021, **16**, 881–893.
19 M.-H. Tsou, *et al.*, Mesoporous silica nanoparticles with fluorescent and magnetic dual-imaging properties to deliver fucoidan, *Int. J. Biol. Macromol.*, 2021, **188**, 870–878.
20 T. H. Lo, *et al.*, Curcumin-loaded mesoporous silica nanoparticles with dual-imaging and temperature control inhibits the infection of Zika virus, *Microporous Mesoporous Mater.*, 2021, **314**.
21 M. H. Tsou, *et al.*, Mesoporous silica nanoparticles with fluorescent and magnetic dual-imaging properties to deliver fucoidan, *Int. J. Biol. Macromol.*, 2021, **188**, 870–878.
22 Z.-H. Lee, *et al.*, Fucoidan with three functions extracted from *Sargassum aquifolium* integrated rice-husk synthesis dual-imaging mesoporous silica nanoparticle, *J. Nanobiotechnol.*, 2022, **20**(1), 298.
23 E. G. Zemtsova, *et al.*, Regulation of the size of metal iron nanoparticles in channels of mesoporous silica matrices (MCM-41, SBA-15) and structure and magnetic properties of the received nanocomposites MCM-41/Fe^0 and SBA-15/Fe^0, *J. Nanopart. Res.*, 2020, **22**(9), 255.
24 V. Krishnan, G. D. Venkatasubbu and T. Kalaivani, Investigation of hemolysis and antibacterial analysis of curcumin-loaded mesoporous SiO_2 nanoparticles, *Appl. Nanosci.*, 2021, 218.
25 J. Yao, *et al.*, Ionic Liquids Grafted Mesoporous Silica for Chemical Fixation of CO_2 to Cyclic Carbonate: Morphology Effect, *Catal. Lett.*, 2022, **152**(3), 781–790.
26 A. Dalal, *et al.*, Red emissive ternary europium complexes: synthesis, optical, and luminescence characteristics, *Luminescence*, 2022, 1–12.
27 M. Santibanez, *et al.*, A high-sensitivity and low dose energy-dispersive X-ray fluorescence system for identification of gadolium accumulations in planar X-ray fluorescence images, *Appl. Radiat. Isot.*, 2019, **151**, 46–51.
28 K. Żamojć, *et al.*, The Development of 1,3-Diphenylisobenzofuran as a Highly Selective Probe for the Detection and Quantitative Determination of Hydrogen Peroxide, *Free Radical Res.*, 2016, **51**, 1–32.
29 D. Jaque, *et al.*, Nanoparticles for photothermal therapies, *Nanoscale*, 2014, **6**(16), 9494–9530.
30 A. S. Kuznetsova, *et al.*, Electrokinetic Characteristics of Bismuth-Containing Materials Based on Porous Glasses, *Glass Phys. Chem.*, 2020, **46**(4), 290–297.
31 M. Skoczylas, S. Bocian and B. Buszewski, Influence of silica functionalization by amino acids and peptides on the stationary phases zeta potential, *J. Chromatogr. A*, 2018, **1573**, 98–106.
32 R. Radwan, *et al.*, Development and Evaluation of Letrozole-Loaded Hyaluronic Acid/Chitosan-Coated Poly(D,L-lactide-*co*-glycolide) Nanoparticles, *J. Pharm. Innov.*, 2021, 439.
33 A. M. Beagan, Investigating Methylene Blue Removal from Aqueous Solution by Cysteine-Functionalized Mesoporous Silica, *J. Chem.*, 2021, **2021**, 1–12.
34 N. Encinas, *et al.*, Mixed-charge pseudo-zwitterionic mesoporous silica nanoparticles with low-fouling and reduced cell uptake properties, *Acta Biomater.*, 2019, **84**, 317–327.
35 N. K. Thakral, *et al.*, Soluplus-Solubilized Citrated Camptothecin-A Potential Drug Delivery Strategy in Colon Cancer, *AAPS PharmSciTech*, 2012, **13**(1), 59–66.
36 S. Grabska-Zielinska, *et al.*, The Characterization of Scaffolds Based on Dialdehyde Chitosan/Hyaluronic Acid, *Materials*, 2021, **14**(17), 4993.
37 A. Gumala, Sutriyo and F. C. Saputri, Characterization and biodistribution of *trans* resveratrol-PEG-folic acid-gold nanoparticle conjugates, *Trop. J. Pharm. Res.*, 2021, **20**(2), 223–230.